APL Materials

RESEARCH ARTICLE | AUGUST 13 2025

The characterization and understanding of electrically active defects in the $HfO_2/\beta\text{-}Ga_2O_3(\bar{2}01)$ MOS system

Khushabu S. Agrawal ; Paolo La Torraca ; Jonas Valentijn ; Roberta Hawkins ; Adam A. Gruszecki ; Joy Roy ; Vasily Lebedev ; Lewys Jones ; Robert M. Wallace ; Chadwin D. Young ; Paul K. Hurley ; Karim Cherkaoui

APL Mater. 13, 081116 (2025)

https://doi.org/10.1063/5.0283247

CHORUS

AIP Publishing

The characterization and understanding of electrically active defects in the $HfO_2/\beta\text{-}Ga_2O_3$ $(\bar{2}01)$ MOS system

Cite as: APL Mater. 13, 081116 (2025); doi: 10.1063/5.0283247
Submitted: 30 May 2025 • **Accepted:** 27 July 2025 •
Published Online: 13 August 2025

Khushabu S. Agrawal,[1] **Paolo La Torraca,**[1] **Jonas Valentijn,**[1] **Roberta Hawkins,**[2,a)] **Adam A. Gruszecki,**[2] **Joy Roy,**[2] **Vasily Lebedev,**[3] **Lewys Jones,**[3] **Robert M. Wallace,**[2] **Chadwin D. Young,**[2] **Paul K. Hurley,**[1,4] **and Karim Cherkaoui**[1,b)]

AFFILIATIONS

[1] Tyndall National Institute, University College Cork, Lee Maltings, Prospect Row, Cork, Ireland
[2] Department of Materials Science and Engineering, The University of Texas at Dallas, Richardson, Texas 75080, USA
[3] Advanced Microscopy Laboratory (AML), School of Physics, CRANN & AMBER Trinity College Dublin, The University of Dublin, Dublin 2, Ireland
[4] The School of Chemistry, University College Cork, Cork, Ireland

[a)] **Current address:** Qorvo, Inc., Richardson, Texas 75080, USA.
[b)] **Author to whom correspondence should be addressed:** karim.cherkaoui@tyndall.ie

ABSTRACT

We have investigated the properties of the $Au/Cr/HfO_2/\beta\text{-}Ga_2O_3(\bar{2}\,01)$ MOS (metal-oxide-semiconductor) system after annealing (450 °C) in different ambient conditions (forming gas, N_2, and O_2). Defect properties have been analyzed using an approach combining experimental impedance measurements with physics-based simulations of the capacitance–voltage (C–V) and conductance–voltage (G–V) characteristics of $\beta\text{-}Ga_2O_3/HfO_2$ MOS capacitors. The analysis demonstrates that the electrically active defects are not confined to the $\beta\text{-}Ga_2O_3/HfO_2$ interface but are comprised of two defect bands in HfO_2 characterized by thermal ionization energies of ~1.1 eV (acceptor-like) and ~2 eV (donor-like) attributed to a polaronic self-trapping state and an oxygen vacancy in HfO_2, respectively. The adopted methodology also enabled the extraction of the spatial distribution of defects across the HfO_2 thickness and Cr/HfO_2 interface. The high concentration of oxygen vacancies close to the Cr/HfO_2 interface extracted from experimental and simulated electrical data is confirmed by *in situ* XPS analysis, which shows how Cr is scavenging oxygen from the HfO_2 and creating the donor band confined near the Cr/HfO_2 interface. This donor band density is observed to be reduced after annealing, and the reduction is not ambient dependent.

I. INTRODUCTION

$\beta\text{-}Ga_2O_3$ has been widely explored for high power applications because of its superior electrical properties compared to SiC and GaN, including a wider bandgap of ~4.8 eV and a high breakdown field that is 2–3 times greater (~8 MV cm^{-1}).[1–4] In addition, the cost-effective production of $\beta\text{-}Ga_2O_3$ is another significant advantage of $\beta\text{-}Ga_2O_3$-based high power device applications. Recent trends in $\beta\text{-}Ga_2O_3$-based metal-oxide-semiconductor devices explore the use of HfO_2, Al_2O_3, and SiO_2 dielectrics.[5–9] The realization of Ga_2O_3 MOS devices faces some severe challenges, such as charge trapping or the absence of hole conduction, which restricts the design to unipolar devices or heterojunctions.

High dielectric constant HfO_2 material has been introduced in the fabrication of Si-based complementary MOS technology, which has enhanced device performance and lowered power consumption. HfO_2 possesses a high dielectric constant (k~16–25),[10,11] relatively high conduction band offsets, and higher barrier heights with respect to gate metals. High-k dielectrics are also desirable for electric field management in lateral power devices;[12–14] therefore, it is noteworthy to consider HfO_2 as a dielectric material for Ga_2O_3-based MOS devices. SiO_2 and Al_2O_3 have lower k values than HfO_2

but offer higher band offsets and higher bandgaps, resulting in lower leakage current and better thermal gate stack stability.[15–17]

The properties of the dielectric/semiconductor and dielectric/metal interfaces have a great impact on the overall electrical properties of the device. Dielectric oxide defects may also significantly alter the device characteristics and reliability. Interface traps and border traps are the most common defects in high-k dielectrics, which can affect shorter/longer term performance degradation of the device. Oxygen vacancies in HfO_2 lead to threshold voltage shifts and even lower the carrier mobility in the channel material.[18] Defects in Al_2O_3 are responsible for Fermi level pinning and a substantial threshold voltage shift in capacitance–voltage (C–V),[19] whereas the interface state density between SiO_2/Ga_2O_3 causes the C–V to stretch out and introduces frequency dispersion in accumulation capacitance.[20]

These defects result from the dielectric deposition process or during treatments after dielectric deposition, such as rapid thermal annealing (RTA),[21] which influences the C–V characteristics. The impact of high temperature process annealing on $HfO_2/\beta\text{-}Ga_2O_3$ has been investigated by Masten *et al.*, and their findings showed how high temperature annealing at 700–850 °C increases the leakage current and density of interface traps.[22] Jayawardhana *et al.* demonstrate how annealing of Ga_2O_3/Al_2O_3 MOS devices at 500 °C for 2 min in forming gas (FG) causes a rise in shallow interface states in comparison with annealing in N_2 ambient.[23] The C–V characteristics of Ga_2O_3 MOS have been reported to exhibit a shift charge trapping instability irrespective of the dielectric used. The charge trapping in the $Al_2O_3/(\bar{2}\,01)Ga_2O_3$ MOS capacitors showed C–V stretch-out and flat band shift after successive voltage sweep capacitance measurements.[23] Chen *et al.* have shown a similar stretch out behavior with ZrO_2 dielectric on Ga_2O_3, which was attributed to interface traps.[24] Further, Zeng *et al.* studied the interface states behavior in SiO_2/Ga_2O_3 MOS capacitors and related this stretch-out and flat-band shift with defect states in the dielectric and at the interface.[20] Commonly reported problems include C–V flat band shifting following consecutive sweeps, C–V stretching, and dispersion in accumulation capacitance where the origin remains unspecified after annealing. Therefore, to progress technology for high power applications using Ga_2O_3-based MOS devices, it is important to investigate the source of these limitations, as annealing is an essential step in the fabrication process.

In this work, we have systematically studied how defects in the $HfO_2/\beta\text{-}Ga_2O_3$ system play a significant role in changing the frequency dependent C–V and conductance–voltage (G–V) properties after annealing in various ambient conditions in comparison with the as-deposited (control sample). A thorough analysis has been conducted, which details how annealing affects the space-energy distribution of traps within hafnia and primarily alters the MOS device's C–V and G–V characteristics. We replicate experimental data using the Ginestra simulation platform, analyzing the distribution of defects in the oxide and interface with Ga_2O_3 and Cr metal. The extracted thermal ionization energy of the two defect bands indicates the presence of an intrinsic polaronic defect near the Ga_2O_3/HfO_2 interface and the oxygen vacancy in HfO_2 near the HfO_2/Cr interface.[25,26] We also investigated the HfO_2/Cr interface with the help of *in situ* X-ray photoelectron spectroscopy (XPS), explaining that Cr is scavenging oxygen from the HfO_2 layer.

II. EXPERIMENTAL METHODS

The MOS structures were fabricated using unintentionally doped $(\bar{2}\,01)$ $\beta\text{-}Ga_2O_3$ semiconductor substrates procured from Novel Crystal Technology, Japan. More information regarding ALD of HfO_2 and wafer pre-cleaning can be found elsewhere.[27] Following the ~12 nm HfO_2 ALD process, the substrate was split into four samples: three samples were subjected to an RTA (post deposition annealing (PDA)) treatment at 450 °C for 5 min in forming gas (5% H_2 + 95% N_2), Oxygen (O_2), and Nitrogen (N_2) ambients, respectively, and one sample was used as a control sample (as-deposited). For all samples, circular contacts with a 200 μm diameter of Cr (20 nm)/Au (150 nm) were formed as top gate electrodes through shadow mask stencils using E-beam evaporation. 20 nm Ti and 150 nm Au layers were deposited as back contacts. BCl_3 etching was carried out prior to Ti/Au metal deposition. The schematic of the $\beta\text{-}Ga_2O_3/HfO_2$/Cr MOS structure is shown in Fig. 1 along with the MOS capacitor process flow. The C–V and G–V measurements were carried out using an Agilent E4980 LCR meter. Each C–V measurement was performed at room temperature in a dark environment at frequencies ranging from 100 Hz to 1 MHz.

The *in situ* XPS characterization was performed by forming the Ga_2O_3/HfO_2(12 nm)/Cr (1 nm) samples in the ultra-high vacuum (UHV) cluster tool. The XPS in the cluster tool is equipped

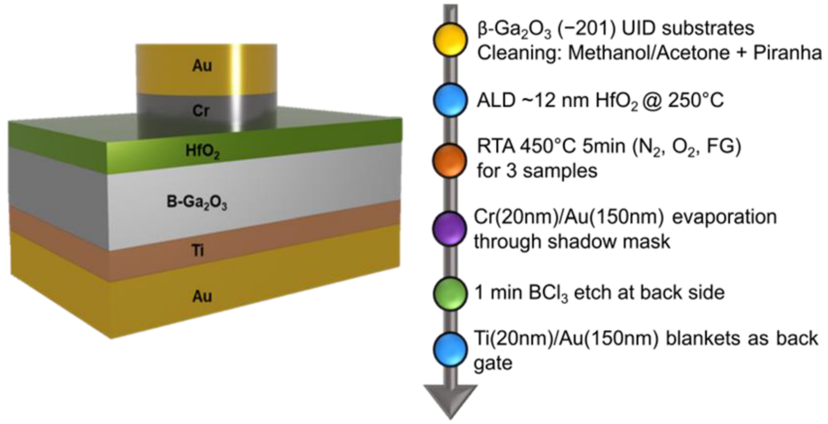

FIG. 1. Schematic diagram of the $Au/Cr/HfO_2/Ga_2O_3$ MOS structure and the fabrication process steps.

with a monochromatic Al Kα source and an Omicron EA125 hemispherical analyzer, achieving a resolution of ±0.05 eV. In this work, XPS was performed in as-loaded conditions and compared with those after subsequent process steps. A reference Cr layer (25 nm) was also deposited under UHV conditions on a SiO_2/Si substrate to compare with the Cr reaction products. The details of the sample preparation are provided in the supplementary material. All the XPS spectra were fitted using Analyzer software.[28] The lithography process was avoided throughout the experiment to maintain clean, *in situ* environments.

The high-resolution transmission electron microscopy (HRTEM) and energy dispersive analysis (EDS) were performed after characterizing the samples electrically. The lamellas were prepared by the TESCAN Solaris Ga+ dual-beam focused ion beam (FIB) system. To protect the region of interest before FIB milling, multiple protecting layers (a 50–100 nm carbon layer, followed by a 300–500 nm platinum layer, and an additional 3.5 μm thick carbon protecting layer for protection) were deposited using electron beam induced deposition. Thinning was performed at 30 kV, with a final low-energy polish at 5 kV (20 pA) to minimize ion beam-induced damage. High-resolution TEM and STEM were performed using an FEI Titan 80–300 microscope (Thermo Fisher Scientific, USA) equipped with a Schottky field-emission gun operated at 300 kV and a HAADF detector for STEM. For high resolution TEM, the electron dose was below 3×10^6 nm^{-2} s^{-1}, minimizing electron beam damage. TEM images were recorded with a Gatan UltraScan CCD camera (Gatan, Inc., USA) and processed using the open source Gwyddion software. EDS mappings were acquired using a Bruker XFlash 6-30 EDS detector (Bruker Co., USA) and processed using the open source HyperSpy library.

Simulations of the MOS capacitor impedance characteristics were performed using the Applied Materials Ginestra simulation platform to extract the defect properties.[29] The software employs the calculation of charge transport, electrostatics in MOS governed by the direct tunneling, and trap assisted tunneling self consistently to/from the charge trapping/emission dynamics of the defects. More importantly, the charge transport phenomenon is modeled according to the multi-phonon trap assisted tunneling theory, which explains the electron–phonon coupling and atomic lattice relaxation associated with the charge trapping systematically. Table I lists the general parameters used to reproduce the experimental results. The doping concentration in Ga_2O_3 was extracted from the $1/C^2$ vs V curve of the as-deposited sample. It is noted that the deep depletion exhibited by the HfO_2/Ga_2O_3 structure facilitates the evaluation of the electrically active dopant concentration into the Ga_2O_3 beyond a nominal maximum depletion depth, as surface inversion cannot be achieved in a Ga_2O_3 MOS device.

TABLE I. Materials parameters used for the C–V and G–V simulations.[3,30–32]

Materials	Properties	Value
β-Ga_2O_3	Bandgap (eV)	4.85
	Electron affinity χ (eV)	4
	Doping N_D (cm^{-3})	1.8×10^{17}
	Relative dielectric permittivity ε	10
	Carrier mobility μ_n (cm^2 V^{-1} s^{-1})	300
Cr	Work function (eV)	4.5
HfO_2	Bandgap (eV)	5.8
	Electron affinity χ (eV)	2.4
	Effective electron tunneling mass m_T	0.25 m_o
	Oxide thickness (nm)	12

III. RESULTS AND DISCUSSION

In the current study, we have observed a significant flat band shift after successive C–V sweeps (Fig. S1 in the supplementary material), which has also been observed by other groups.[22,33–35] This flat band shift, which we attribute to trapped charge upon successive voltage sweeps, is still present several days after the initial measurement (the systematic study of the trapped charge dynamics over time is beyond the scope of this paper). The origin of this behavior has not been extensively discussed in the literature, and it is important to examine some of the causes of this behavior in the high-k/Ga_2O_3 system. We believe that this *semi-permanent* charge trapping effect is not only caused by the presence of defect states located deep in the dielectric presenting high thermal activation energy, but this effect is also strongly dependent on the electric field distribution across the high-k/Ga_2O_3 device. In MOS capacitors, including conventional semiconductors (energy bandgap <2 eV), the electric field across the dielectric for a given bias in the inversion region is comparable with the field when the device is in the accumulation region. For Ga_2O_3 MOS devices, the situation is different, as the semiconductor does not invert due to its wide bandgap of 4.85 eV, which gives rise to asymmetry in the electric field. The applied bias in depletion drops across the dielectric and Ga_2O_3, which results in strong electric field asymmetry between the accumulation and depletion conditions of the MOS system. This situation is compounded by the higher k value of HfO_2 (16) than the k value of Ga_2O_3 (10). To investigate this, we have simulated the electric fields in the inversion regime of HfO_2 on Si and HfO_2 on Ga_2O_3 MOS capacitors by considering zero defects in HfO_2 (ideal case). Figure 2 compares the electric field across both systems at a specified bias of −2 V, which is in the depletion (or inversion) mode of the MOS device. A Cr metal gate was assumed for the simulation, and the n-type doping levels in Si and Ga_2O_3

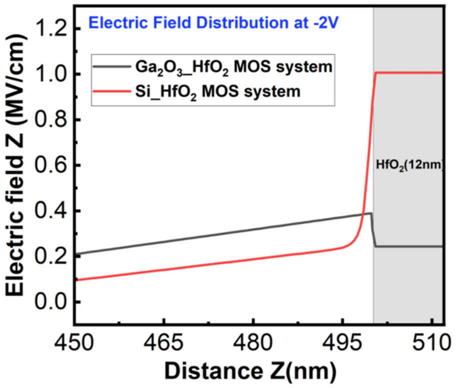

FIG. 2. Electric field distribution of the Cr/HfO_2/Si and Cr/HfO_2/Ga_2O_3 MOS systems plotted in the depletion/inversion region at −2 V. The simulation is performed without considering any defects (ideal mode). Z is the distance in nm; HfO_2 thickness is the same for both systems.

(2×10^{17} cm^{-3}) and semiconductor affinity values were very similar (4 eV), which allows the comparison of the electric field across both structures for a given applied bias. At −2 V in depletion/inversion, the electric field in HfO_2 is ~5 times lower for the Ga_2O_3 MOS structure in comparison with the HfO_2 field for the Si device. In MOS devices, C–V sweeps from depletion to accumulation may cause free carriers in the semiconductor to be trapped in the dielectric. This charge trapping is driven by the electric field across the dielectric. In the case of successive C–V sweep measurements, as the bias is brought back to depletion, not all trapped charge is recovered, causing flat band shifts or producing hysteresis in double C–V sweeps (e.g., negative to positive bias and back). This effect is more pronounced in HfO_2/Ga_2O_3 MOS devices because the voltage in deep depletion is split between the Ga_2O_3 and the HfO_2, resulting in a lower field across the dielectric in depletion and, therefore, less recovery of trapped charge. The large C–V shifts observed in high-k/Ga_2O_3 MOS devices as compared to high-k/Si are not necessarily caused by higher dielectric trap concentrations or different defect thermal ionization.

Figures 3 and 4 show the experimental C–V and G–V data curves for all four samples, namely as-deposited, forming gas, N_2 and O_2 ambient annealed, respectively, measured at room temperature. These are the initial C–V and G–V curves measured at different frequencies (100 Hz to 1 MHz) using the frequency sweep mode. In frequency sweep mode, the measurement frequency is swept for every gate voltage. The bias is incremented by 0.1 V at each step, and then capacitance and conductance values are taken at different frequencies. This will ensure that all frequency measurements are recorded in a single bias sweep and that the multi-frequency characteristics receive an identical bias stress at each bias point. The difference between using the frequency sweep mode as described earlier and the more conventional voltage sweep mode is shown in the supplementary material (S1).

The as-deposited C–V curve [Fig. 3(a)] shows significant frequency dispersion in accumulation. This dispersion is related to the capture and emission process of majority carriers by oxide traps located close to the oxide/semiconductor interface, while the parallel flat band shift toward positive voltage is associated with the negative oxide charge (fixed or trapped charge). As shown in Fig. 3(b), an increase in frequency dispersion and C–V stretch out after PDA in forming gas ambient for 5 min was observed. The relative flat band shift and decrease in accumulation capacitance after the PDA are also noted. Further stretch out in the C–V, an increase in frequency dispersion, and a positive flat band voltage shift and a decrease in accumulation capacitance were observed for N_2 and O_2 annealed samples as shown in Figs. 3(c) and 3(d), respectively. This reveals the degradation of the HfO_2 properties and the generation of more defects in the oxide due to the PDA. The respective G–V characteristics for all four samples are also shown in Figs. 4(a)–4(d). Noticeably, the acquired G–Vs show the effects of non-idealities in the negative voltage range (i.e., in deep-depletion), ascribed to the impedance measurements inherent limitations. In the presence of the wide Ga_2O_3 depletion region, corresponding to a small and non-lossy capacitance, the used instrumentation is at the limit of its accuracy and may acquire both noisy (at $f < 1$ kHz) and negative conductance values, the latter being removed from the G–V plots. Nonetheless, the noiseless positive readings provide information on the negative bias conductance, showing a decrease in conductance values for the annealed samples compared to the control sample.

To extract the defect properties in HfO_2 for all four samples, we used Ginsetra, which implements a multi-phonon trap assisted

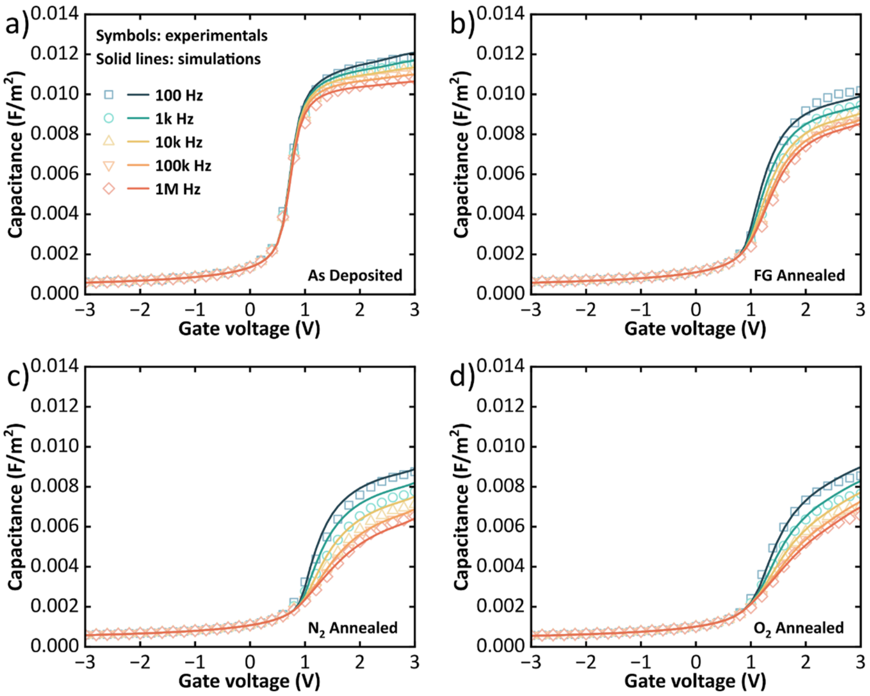

FIG. 3. Capacitance voltage (C–V) curves of Au/Cr/HfO_2/Ga_2O_3 MOS systems measured at multiple frequencies at 295 K: (a) as deposited, (b) forming gas annealed, (c) N_2 annealed, and (d) O_2 annealed. The experimental data are shown in symbols, while solid lines show the simulated data.

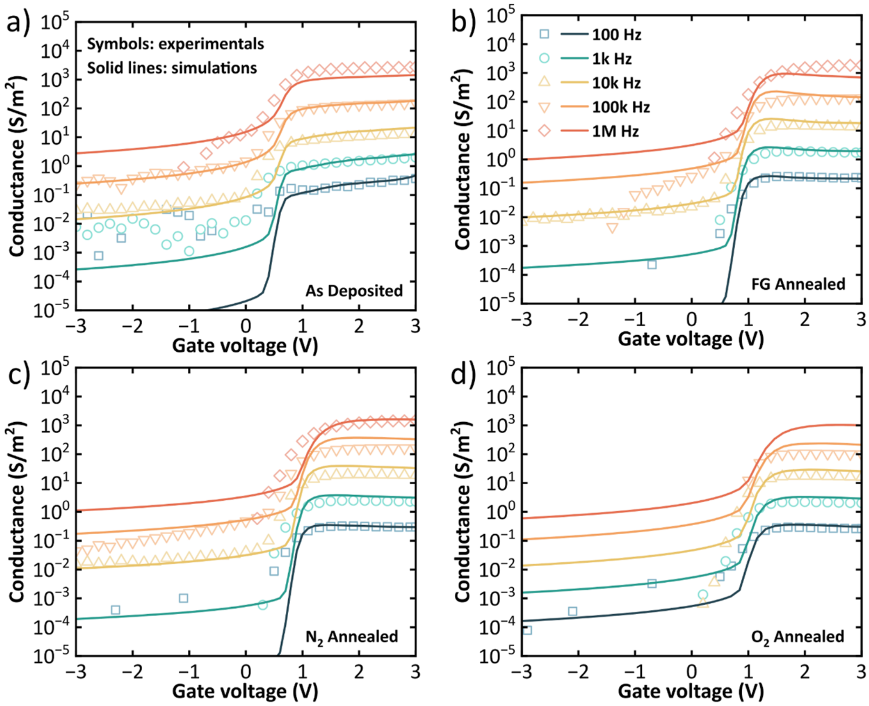

FIG. 4. Corresponding conductance–voltage (G–V) curves of Au/Cr/HfO_2/Ga_2O_3 MOS systems measured at multiple frequencies at 295 K: (a) as deposited, (b) forming gas annealed, (c) N_2 annealed, and (d) O_2 annealed. The experimental data are shown in symbols, while solid lines show the simulated data.

tunneling (MPTAT) model.[36] In this framework, the active defects are characterized by a capture cross section σ, phonon energy ħω, Huang–Rhys factor S, tunneling mass m_T, and trap levels localized in energy and space $E_{T,Z}$.[37] The relaxation energy E_{REL} determines the capture emission time constant and temperature dependence, which is useful to identify the physical nature of the defects. The parameters utilized for simulation are listed in Table I. It is well established that the oxygen vacancies are common bulk defects

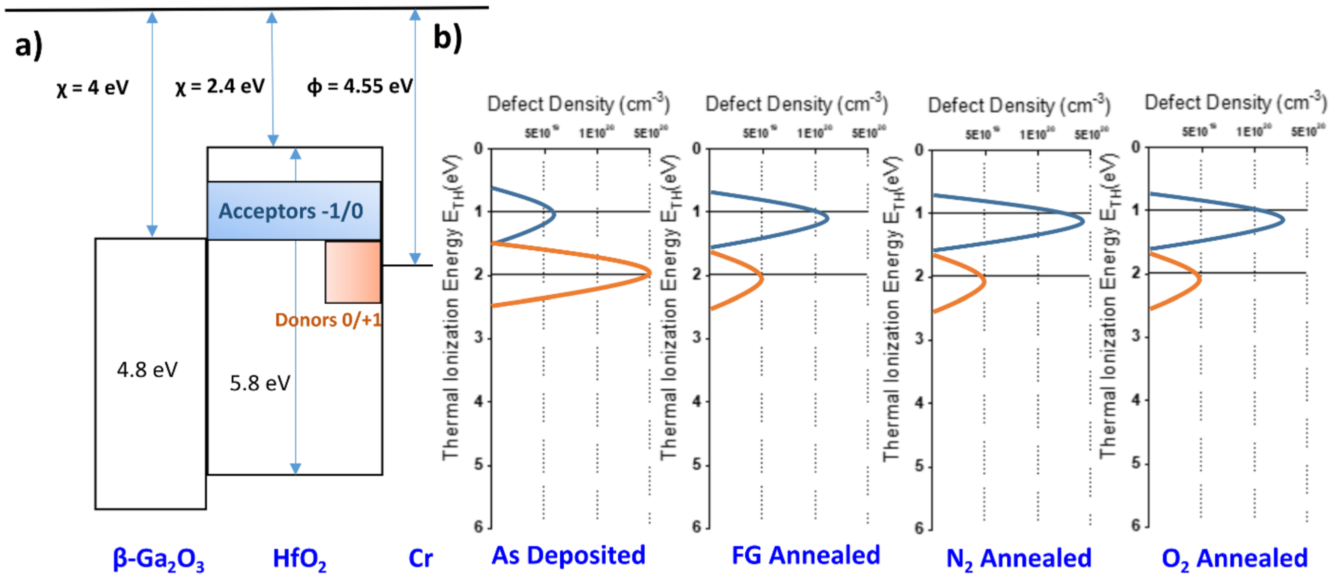

FIG. 5. Defect distribution extracted for the Au/Cr/HfO_2/Ga_2O_3 MOS system. (a) Band diagram of the Cr/HfO_2/Ga_2O_3 stack with two distinct defect distributions: the acceptor band is distributed throughout the HfO_2 thickness, while the donor band is confined near the HfO_2/Cr interface. (b) Defect volume density of the acceptor and donor bands plotted as a function of thermal ionization energy for as deposited, FG annealed, N_2 annealed, and O_2 annealed samples.

in HfO_2 causing the degradation of its dielectric properties and distort electrical characteristics in MOS devices.[21,38,39] The quantitative energy-space distributions of traps causing the degradation in experimental C–V were simulated by considering different traps taking part in the degradation process. We have considered two defect bands to match the experimental C–V and G–V characteristics: an acceptor-like band likely distributed across the full HfO_2 thickness and a donor-like band spatially localized near the Cr electrode, as shown in Fig. 5(a). Both acceptor-like (0/−1) and donor-like (+1/0) traps were considered for simulating the C–V and G–V and reproducing the experimental data in Figs. 3 and 4.

The defect energy distributions were extracted for all samples and plotted in Fig. 5(b) with the main defect parameters summarized in Table II. Figure 3 also compares the experimental C–V characteristics (symbols) with the simulated C–V (solid lines) for all four samples by considering a defect energy distribution ~1.1 eV below the HfO_2 conduction band (Ec). Another defect band (donor-like) about 2 eV below the conduction band of HfO_2 is required to produce the best match with experimental G–V for the gate bias in the deep depletion region as shown in Figs. 4(a)–4(d). It is important to note that the acceptor band required to explain the multi-frequency C–V behavior in accumulation does not necessarily need to extend across the full HfO_2 thickness. At the bias, temperature, and frequency measurement conditions, electrons are only able to communicate with defects located up to ~5 nm from the HfO_2/Ga_2O_3 interface. However, the intrinsic acceptor-like traps are likely to be distributed across HfO_2 and this assumption has no effect on the simulated C–V and G–V characteristics. The donor band, however, is found not to be uniformly spatially distributed. The donor-like traps are present up to 3 nm from the Cr interface; this constraint is imposed by the C–V characteristic, which is not matched with a uniform donor distribution.

The defect density (acceptor and donor) varies between 5×10^{19} and 5×10^{20} cm^{-3} for all four samples, while an E_{REL} value of 1–1.2 eV was used for the simulation. To match the experimental data with the simulation, different *k* values were required. It is worth noting that a k value of 17 gives the best match for the as-deposited sample, while *k* values in the range of 13–16 give the best match for forming gas, N_2 and O_2 samples. Such low-*k* values for HfO_2 are unexpected, and the possible origin will be discussed further below.

Figure 5(b) summarizes the effect of annealing conditions on the defect distribution over energy and space within the bandgap of HfO_2. It is observed that the peak density for the donor defects remains constant before and after thermal treatment, while the density strongly decreases after the annealing for all ambient conditions. The acceptor density, however, increased significantly post thermal annealing, associated with a slight increase in thermal ionization energy spread. The two effects combined result in more defect states aligned with the Ga_2O_3 conduction band and, therefore, an increased frequency dispersion in the C–V response after annealing.

Many studies on the application of HfO_2 dielectric in MOS devices confirm that one of the most prevalent defects currently observed is oxygen vacancies. These oxygen vacancies play an important role in generating trapping sites in MOS devices.[18,26] Annealing significantly influences these defects by modifying the material properties and inducing a phase transition in HfO_2.[40,41] In addition, the concentration of these oxygen vacancies seems to be phase dependent. The amorphous HfO_2 tends to have significant oxygen vacancies due to a less ordered structure, while the phase

TABLE II. Extracted defect parameters for HfO_2 based on simulation results.

Sample	Dielectric constant (*k*)	Acceptor defect	Donor defect
Phonon energy (E_{PH})	⋯	0.03 eV	0.06 eV
Capture cross section (σ)	⋯	5×10^{-17} cm^2	10^{-14} cm^2
As deposited	17	E_{th}: 1.1 eV E_{rel}: 1 eV Std dev = 0.2 eV Defect density: 6×10^{19} cm^{-3}	E_{th}: 2 eV E_{rel}: 1.2 eV Std dev = 0.1 eV Defect density: $5 \times 10^{20} cm^{-3}$
Forming gas annealed	16	E_{th}:1.1 eV $E_{rel:}$ 1 eV Std dev = 0.25 eV Defect density: 2×10^{20} cm^{-3}	E_{th}: 2 eV E_{rel}: 1.2 eV Std dev = 0.1 eV Defect density: 5×10^{19} cm^{-3}
N_2 annealed	14	E_{th}:1.1 eV E_{rel}: 1 eV Std dev = 0.25 eV Defect density: 4×10^{20} cm^{-3}	E_{th}: 2 eV E_{rel}: 1.2 eV Std dev = 0.1 eV Defect density: 5×10^{19} cm^{-3}
O_2 annealed	13	E_{th}: 1.17 eV E_{rel}: 1.12 eV Std dev = 0.2 eV Defect density: 3.5×10^{20} cm^{-3}	E_{th}: 2 eV E_{rel}: 1.2 eV Std dev = 0.1 eV Defect density: 5×10^{19} cm^{-3}

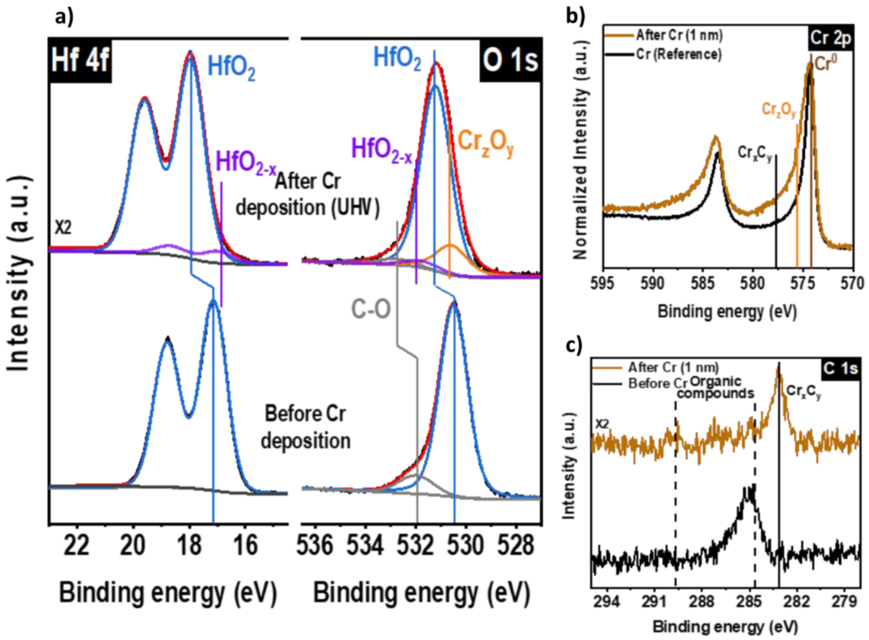

FIG. 6. *In situ* XPS of the Cr/HfO$_2$ interface on the β-Ga$_2$O$_3$ ($\bar{2}$01) bulk substrate with 12 nm of ALD-grown HfO$_2$: (a) Hf 4*f* O 1*s*, (b) Cr 2*p*, and (c) C 1s interface chemistry before and after UHV Cr gate metal deposition. Intensities are multiplied 2x after the Cr deposition as the overlayer obscures the underlying elemental states.

transition to cubic may have more oxygen vacancy tolerance.[38,42] Another source of trapping states in both amorphous and crystalline HfO$_2$ are polaronic states, originating from the strong interaction between charge carriers and the lattice vibrations (i.e., phonons) in the material. The oxygen vacancy may exist in +2, +1, 0, −1, and −2 states. The +2 and +1 states are deep trap states, while the neutral state is expected to occur positioned ~1 eV below the CB minima.[25] These defects are common in HfO$_2$ regardless of the substrate on which it is deposited.

The donor defect band distributed near the Cr interface could be explained by the strong oxygen affinity of Cr when deposited on HfO$_2$ or other oxides and could lead to oxygen scavenging from HfO$_2$ and increase the V$_\text{O}$ density locally.[43,44] *In-situ* XPS analysis was performed on the Cr/HfO$_2$/Ga$_2$O$_3$ stack to provide more in-depth chemical information about the Cr/HfO$_2$ interface.

Figure 6 shows the XPS results before and after Cr deposition on HfO$_2$ dielectric grown on β-Ga$_2$O$_3$ ($\bar{2}$ 01) substrate (without annealing: control sample). Since the substrate signal was below the detection limit of XPS (see the supplementary material, Fig. S2: survey spectra), only the interface between Cr and HfO$_2$ is analyzed. Peak positions are referenced to the C 1s (284.8 eV) peak to minimize charging effects observed after oxide growth. Figure 6(a) shows the Hf 4f and O 1s core level peaks after ALD deposition and following UHV metallization. Signals detected in both Hf 4f at 17.3 eV and O 1s at 530.4 eV binding energy (BE) denote the HfO$_2$ state.[45,46] The sub-stoichiometric state is below the detection limit of XPS for the HfO$_2$ surface. C and O 1s show surface organic impurities likely sourced from the ALD chamber where metal-organic precursors are used. C1s in Fig. 6(c) demonstrates a small amount of carbon compounds at the surface consistent with O 1s.[47] No carbide species (~282 eV)[48] was detected following ALD deposition.

However, after Cr deposition, multiple reactions were observed at the Cr/HfO$_2$ interface compared to reference Cr [see Fig. 6(b) "Cr (Reference)"]. In Fig. 6(a), the full width at half maximum (FWHM) of Hf 4f increased by 0.12 eV after 1 nm Cr deposition, and a shoulder peak near the lower BE site appeared. Similar changes are observed in O 1s, suggesting a reduction of HfO$_2$ by Cr and the formation of a sub-stoichiometric (HfO$_{2-x}$) state. Cheng *et al.* reported a similar sub-stoichiometric state in the HfO$_2$/GaN interface.[49] Although thermodynamically HfO$_2$ is more stable than chromium oxides (approximate standard Gibbs-free energy, $\Delta G^\circ{}_f$, HfO$_2$ 548.5 kJ/mol per bond of Hf–O and $\Delta G^\circ{}_f$, Cr$_2$O$_3$ = -379.7 kJ/mol per bond of Cr–O),[50] amorphous HfO$_2$ has a less stable atomic structure with higher defect densities.[51] This can alternatively make oxygen more mobile and easier to scavenge by Cr. Moreover, metal-induced defect states can also be responsible for such an oxygen scavenging effect.[52] Cr 2p in Fig. 6(b) shows multiple oxidation states compared to the reference Cr metal. Along with metallic Cr^0 states, oxides and carbides[53] are also detected in Cr 2p. O 1s (530.6 eV) and C 1s (~283.3 eV) show the Cr oxide and carbide,[54] respectively, suggesting the presence of aggressive reactions at the HfO$_2$/Cr interface.

A shift toward higher binding energy values in Hf 4f and O1s spectra was observed after metal deposition. The scavenging of oxygen from HfO$_2$ creates oxygen vacancies or related donor states, which may eventually shift the oxide's Fermi level (E$_\text{F}$) toward the conduction band.[18,55] In addition, dipole formation at the Cr/HfO$_2$ interface might also induce some BE shift.[56] The Cr Fermi level alignment could also induce downward HfO$_2$ band bending and contribute to the BE shift.

Considering the effect of thermal annealing on the defect bands, the donor concentration is reduced by one order of magnitude after annealing but is unaffected by the different annealing conditions [as depicted in Fig. 5(b)]. It seems the annealed HfO$_2$ films react less with Cr as compared to the as-deposited films (*in situ* XPS analysis on annealed HfO$_2$ was not available for this study). On

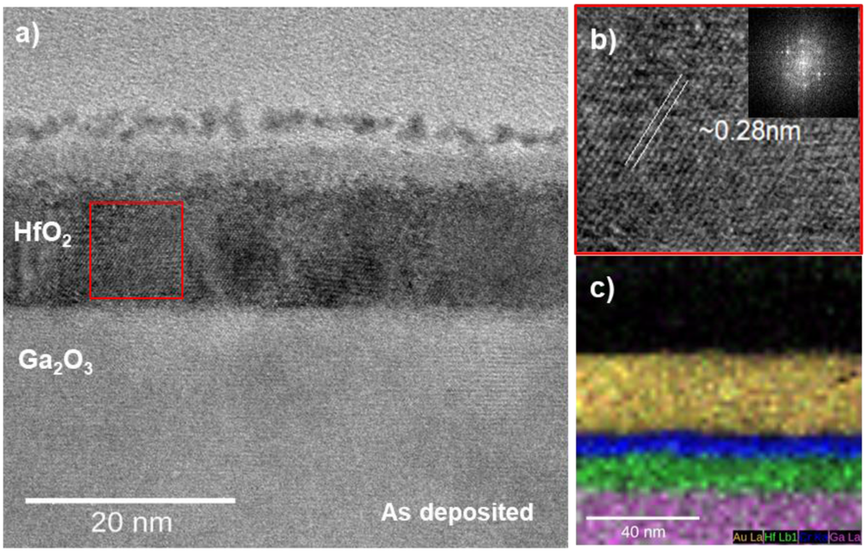

FIG. 7. (a) High-resolution cross-sectional TEM images of the as-deposited Au/Cr/HfO$_2$(12 nm)/Ga$_2$O$_3$ MOS. The observed HfO$_2$ layer thickness for all four samples is ~11.5 ± 0.5 nm (Fig. S3). (b) Zoomed area of the red square of the image (a); the inset shows the respective FFT micrograph. (c) Elemental analysis of Au/Cr/HfO$_2$/Ga$_2$O$_3$ MOS layers using x-ray energy dispersive spectroscopy (EDS) for the as-deposited sample. Ga diffusion into the HfO$_2$ layer is not observed or is below the detection limit in all the acquired maps. Note the absence of Cr above HfO$_2$ for the as-deposited sample because the TEM image was obtained outside the capacitor area.

the other hand, the acceptor defect density is observed to increase for the annealed samples as compared to the control sample. Furthermore, N$_2$ and O$_2$ annealing conditions generate a greater number of acceptor defects than the FG annealed sample. The extracted trap distribution 1.1 eV below Ec supports the attribution of the acceptor to the polaronic defect in HfO$_2$[21,57] associated with under-coordinated Hf ions or elongated Hf–O bonds. While annealing in an oxygen-rich environment could potentially hamper the formation of under-coordinated Hf ions (or even reduce their density), the extracted acceptor trap profiles do not show significant differences associated with the O$_2$ annealing. This can be explained either by the absence of under-coordinated Hf ions in the acceptor trap band or by the annealing time and the thermal budget being insufficient for counteracting the formation of under-coordinated Hf ions. Noticeably, in the former case the acceptor trap band would be mainly composed of elongated Hf–O bonds. The exact explanation of this phenomenon remains unclear and worthy of further investigation.

The *k* value is observed to be dependent on the annealing conditions (17 for as deposited and 13 for O$_2$ annealed). Cross-sectional TEM images of the as-deposited and annealed films (Figs. 7 and S3) confirm the thickness of the HfO$_2$ layer is ~11.5 ± 0.5 nm for all four samples and show no evidence of interlayer formation between the Ga$_2$O$_3$ and HfO$_2$ and rule out HfO$_2$ thickness variation after annealing. The low HfO$_2$ *k* value extracted cannot be attributed to higher than nominal HfO$_2$ physical thickness. It is interesting to note that both as-deposited and annealed samples seem to be polycrystalline in nature. The fast Fourier transform patterns were analyzed to assess the value of the observed interplanar distances of the HfO$_2$ films. An observed d-spacing of ~0.28 nm is in good agreement with the literature data for crystalline HfO$_2$ (Fig. S3).[7,58] The extracted *k* value of 17 for the as-deposited sample is consistent with the monoclinic phase reported by several groups for HfO$_2$ on Si;[59,60] however, the cause for the lower *k* value (13–16) of the other samples is unclear. Ga diffusion into HfO$_2$ was observed previously in HfO$_2$/Ga$_2$O$_3$ samples annealed at high temperature;[22] however, EDS analysis does not reveal any significant Ga diffusion into HfO$_2$ in our samples. A possible source of the *k* value degradation could be the partial oxidation of the Cr layer in contact with HfO$_2$ (Figs. S4 and S5).

IV. CONCLUSION

We have characterized electrically active defects in the HfO$_2$/$(\bar{2}01)$β-Ga$_2$O$_3$ system. The approach we have adopted, which combines the experimental electrical characteristics with physics-based simulation of MOS devices, was successful in profiling active defects in Au/Cr/HfO$_2$/Ga$_2$O$_3$ MOS devices. Two distinct defect bands with thermal ionization energies ~1.1 and ~2 eV below the HfO$_2$ conduction band have been extracted. The acceptor band at E_{th} = 1.1 eV has been associated with polaronic intrinsic defects in HfO$_2$ in good agreement with the earlier reports; its density and thermal ionization energy spread are observed to be increasing after annealing in different conditions, while the donor band with E_{th} = 2 eV has been associated with the oxygen vacancy donor level in HfO$_2$, which is reduced after annealing and unchanged in different annealing conditions. This defect band is mainly localized near the HfO$_2$/Cr interface, indicating that Cr may be at the origin of this defect by reducing the HfO$_2$ and generating oxygen vacancies. This hypothesis was supported by *in situ* XPS analysis. The study shows how thermal treatment degrades the properties of HfO$_2$/Ga$_2$O$_3$ MOS capacitors and provides useful insights for the selection of process parameters and materials for future Ga$_2$O$_3$ based devices.

SUPPLEMENTARY MATERIAL

The supplementary material encompasses first experimental C–V successive sweeps (Fig. S1); XPS sample preparation and survey spectra scan (Fig. S2); and TEM and EDS characterization: cross-sectional TEM images for all four (control and annealed) samples showing the polycrystalline HfO$_2$ (Fig. S3). Compositional elemental mapping of different layers with EDS intensity normalized spectra (Fig. S4). Cumulative EDS spectra (Fig. S5).

ACKNOWLEDGMENTS

The authors gratefully acknowledge Brendan Sheehan and Davinder Singh from the Tyndall National Institute for FIB preparation of the TEM samples. TEM microscopy characterization and analysis were performed at the CRANN Advanced Microscopy Laboratory, a Research Ireland supported imaging and analysis center. The Tyndall National Institute is supported by Research Ireland under the US-Ireland Research and Development Partnership (Grant No. 21/US/3755). The University of Texas at Dallas is supported by the National Science Foundation through the US-Ireland R&D Partnership Program, Award No. ECCS 2154535. Vasily Lebedev is supported by Research Ireland Grant No. SFI/21/US/3785, and Lewys Jones is supported by Research Ireland Grant Nos. 12/RC/2278_P2 and URF/RI/191637.

AUTHOR DECLARATIONS

Conflict of Interest

The authors have no conflicts to disclose.

Author Contributions

Khushabu S. Agrawal: Conceptualization (equal); Data curation (equal); Formal analysis (equal); Investigation (equal); Methodology (equal); Software (equal); Writing – original draft (equal). **Paolo LaTorraca**: Formal analysis (equal); Investigation (equal); Software (equal); Validation (equal); Writing – review & editing (equal). **Jonas Valentijn**: Methodology (supporting); Resources (supporting). **Roberta Hawkins**: Methodology (supporting); Resources (supporting). **Adam A. Gruszecki**: Methodology (supporting); Resources (supporting). **Joy Roy**: Methodology (equal); Resources (equal); Writing – original draft (supporting). **Vasily Lebedev**: Formal analysis (supporting); Methodology (supporting). **Lewys Jones**: Resources (equal). **Robert M. Wallace**: Supervision (supporting); Validation (supporting); Writing – review & editing (supporting). **Chadwin D. Young**: Supervision (supporting); Validation (supporting); Writing – review & editing (supporting). **Paul K. Hurley**: Supervision (supporting); Writing – review & editing (supporting). **Karim Cherkaoui**: Formal analysis (equal); Funding acquisition (lead); Project administration (lead); Supervision (lead); Validation (lead); Writing – review & editing (supporting).

DATA AVAILABILITY

The data that support the findings of this study are available from the corresponding author upon reasonable request.

REFERENCES

[1] J. Zhang, J. Shi, D.-C. Qi, L. Chen, and K. H. L. Zhang, "Recent progress on the electronic structure, defect, and doping properties of Ga_2O_3," APL Mater. **8**(2), 020906 (2020).

[2] S. J. Pearton, J. Yang, P. H. Cary, F. Ren, J. Kim, M. J. Tadjer, and M. A. Mastro, "A review of Ga_2O_3 materials, processing, and devices," Appl. Phys. Rev. **5**(1), 011301 (2018).

[3] J. Y. Tsao, S. Chowdhury, M. A. Hollis, D. Jena, N. M. Johnson, K. A. Jones, R. J. Kaplar, S. Rajan, C. G. Van De Walle, E. Bellotti, C. L. Chua, R. Collazo, M. E. Coltrin, J. A. Cooper, K. R. Evans, S. Graham, T. A. Grotjohn, E. R. Heller, M. Higashiwaki, M. S. Islam, P. W. Juodawlkis, M. A. Khan, A. D. Koehler, J. H. Leach, U. K. Mishra, R. J. Nemanich, R. C. N. Pilawa-Podgurski, J. B. Shealy, Z. Sitar, M. J. Tadjer, A. F. Witulski, M. Wraback, and J. A. Simmons, "Ultrawide-bandgap semiconductors: Research opportunities and challenges," Adv. Electron. Mater. **4**(1), 1600501 (2018).

[4] A. J. Green, J. Speck, G. Xing, P. Moens, F. Allerstam, K. Gumaelius, T. Neyer, A. Arias-Purdue, V. Mehrotra, A. Kuramata, K. Sasaki, S. Watanabe, K. Koshi, J. Blevins, O. Bierwagen, S. Krishnamoorthy, K. Leedy, A. R. Arehart, A. T. Neal, S. Mou, S. A. Ringel, A. Kumar, A. Sharma, K. Ghosh, U. Singisetti, W. Li, K. Chabak, K. Liddy, A. Islam, S. Rajan, S. Graham, S. Choi, Z. Cheng, and M. Higashiwaki, "β-Gallium oxide power electronics," APL Mater. **10**(2), 029201 (2022).

[5] Y. Yuan, W. Hao, W. Mu, Z. Wang, X. Chen, Q. Liu, G. Xu, C. Wang, H. Zhou, Y. Zou, X. Zhao, Z. Jia, J. Ye, J. Zhang, S. Long, X. Tao, R. Zhang, and Y. Hao, "Toward emerging gallium oxide semiconductors: A roadmap," Fund. Res. **1**(6), 697–716 (2021).

[6] S. Yan, G. Yang, H. He, Q. Liu, Q. Peng, J. Chen, M. Li, Y. Lu, and Y. He, "High-performance self-driven solar-blind ultraviolet photodetectors based on $HfZrO_2/\beta\text{-}Ga_2O_3$ heterojunctions," ACS Appl. Mater. Interfaces **15**(18), 22263–22273 (2023).

[7] Y.-C. Li, T. Huang, X.-X. Li, X.-N. Zhu, D. W. Zhang, and H.-L. Lu, "Domain switching characteristics in Ga-Doped HfO_2 ferroelectric thin films with low coercive field," Nano Lett. **24**(22), 6585–6591 (2024).

[8] Y. Zhang, R. Zhu, W. Huo, H. Liang, and Z. Mei, "Border trap-enhanced Ga_2O_3 nonvolatile optoelectronic memory," Nano Lett. **24**(45), 14398–14404 (2024).

[9] M. Schowalter, A. Karg, M. Alonso-Orts, J. A. Bich, S. Raghuvansy, M. S. Williams, F. F. Krause, T. Grieb, C. Mahr, T. Mehrtens, P. Vogt, A. Rosenauer, and M. Eickhoff, "Composition and strain of the pseudomorphic α-phase intermediate layer at the Ga_2O_3/Al_2O_3 interface," APL Mater. **12**(9), 091104 (2024).

[10] B. Wang, W. Huang, L. Chi, M. Al-Hashimi, T. J. Marks, and A. Facchetti, "High-k Gate dielectrics for emerging flexible and stretchable electronics," Chem. Rev. **118**(11), 5690–5754 (2018).

[11] J.-h. Baek, W.-h. Choi, H. Kim, S. Cheon, Y. Byun, W. Jeon, and J.-S. Park, "Plasma-enhanced atomic layer deposited HfO_2 films using a novel heteroleptic cyclopentadienyl-based Hf precursor," Ceram. Int. **47**(20), 29030–29035 (2021).

[12] D. Misra, H. Iwai, and H. Wong, "High-k gate dielectrics," Electrochem. Soc. Interface **14**(2), 30–34 (2005).

[13] D. I. Shahin, M. J. Tadjer, V. D. Wheeler, A. D. Koehler, T. J. Anderson, C. R. Eddy, and A. Christou, "Electrical characterization of ALD HfO_2 high-k dielectrics on (2−01) $\beta\text{-}Ga_2O_3$," Appl. Phys. Lett. **112**(4), 042107 (2018).

[14] J. Robertson, "High dielectric constant oxides," Eur. Phys. J. Appl. Phys. **28**(3), 265–291 (2004).

[15] G. D. Wilk, R. M. Wallace, and J. M. Anthony, "High-κ gate dielectrics: Current status and materials properties considerations," J. Appl. Phys. **89**(10), 5243–5275 (2001).

[16] Z. Lin, C. Song, T. Liu, J. Shao, and M. Zhu, "Comparative study of plasma-enhanced-atomic-layer-deposited $Al_2\ O_3/HfO_2/SiO_2$ and $HfO_2/Al_2\ O_3/SiO_2$ tri-layers for ultraviolet laser applications," ACS Appl. Mater. Interfaces **16**(24), 31756–31767 (2024).

[17] R. N. Kim, H. W. Yun, J. Lee, and W.-B. Kim, "Dipole formation and electrical properties according to SiO_2 layer thickness at an Al_2O_3/SiO_2 interface," J. Phys. Chem. C **125**(26), 14486–14492 (2021).

[18] A. Kumar, S. Mondal, and K. S. R. Koteswara Rao, "Probing the oxygen vacancy associated native defects in high-κ HfO_2 using deep level transient spectroscopy," J. Appl. Phys. **135**(4), 045305 (2024).

[19] M. Y. Yang, K. Kamiya, and K. Shiraishi, "Interstitial oxygen induced Fermi level pinning in the Al_2O_3-based high-k MISFET with heavy-doped n -type poly-Si gates," AIP Adv. **3**(10), 102113 (2013).

[20] K. Zeng, Y. Jia, and U. Singisetti, "Interface State Density in Atomic Layer Deposited $SiO_2/Ga_2O_3(2{-}01)$ MOSCAPs," IEEE Electron Device Lett. **37**(7), 906–909 (2016).

[21] S. R. Bradley, A. L. Shluger, and G. Bersuker, "Electron-injection-assisted generation of oxygen vacancies in monoclinic HfO_2," Phys. Rev. Appl. **4**(6), 064008 (2015).

[22] H. N. Masten, J. D. Phillips, and R. L. Peterson, "Effects of high temperature annealing on the atomic layer deposited $HfO_2/\beta\text{-}Ga_2O_3(010)$ interface," J. Appl. Phys. **131**(3), 035106 (2022).

[23] A. Jayawardena, R. P. Ramamurthy, A. C. Ahyi, D. Morisette, and S. Dhar, "Interface trapping in (2−01) β-Ga_2O_3 MOS capacitors with deposited dielectrics," Appl. Phys. Lett. **112**(19), 192108 (2018).

[24] J. Chen, H. Qu, J. Sui, X. Lu, and X. Zou, "Relaxation kinetics of interface states and bulk traps in atomic layer deposited ZrO_2/β-Ga_2O_3 metal-oxide-semiconductor capacitors," J. Appl. Phys. **135**(8), 085702 (2024).

[25] R. A. Izmailov, J. W. Strand, L. Larcher, B. J. O'Sullivan, A. L. Shluger, and V. V. Afanas'ev, "Electron trapping in ferroelectric HfO_2," Phys. Rev. Mater. **5**(3), 034415 (2021).

[26] D. Muñoz Ramo, J. L. Gavartin, A. L. Shluger, and G. Bersuker, "Spectroscopic properties of oxygen vacancies in monoclinic HfO_2 calculated with periodic and embedded cluster density functional theory," Phys. Rev. B **75**(20), 205336 (2007).

[27] R. Hawkins, X. Wang, N. Moumen, R. M. Wallace, and C. D. Young, "Impact of process anneals on high-k/β-Ga_2O_3 interfaces and capacitance," J. Vac. Sci. Technol. A **41**(2), 023203 (2023).

[28] XPS Oasis, (n.d.).

[29] Applied Materials Ginestra, (n.d.).

[30] A. Bhattacharyya, C. Peterson, T. Itoh, S. Roy, J. Cooke, S. Rebollo, P. Ranga, B. Sensale-Rodriguez, and S. Krishnamoorthy, "Enhancing the electron mobility in Si-doped (010) β-Ga_2O_3 films with low-temperature buffer layers," APL Mater. **11**(2), 021110 (2023).

[31] D. Guo, Q. Guo, Z. Chen, Z. Wu, P. Li, and W. Tang, "Review of Ga_2O_3-based optoelectronic devices," Mater. Today Phys. **11**, 100157 (2019).

[32] Electron workfunction of the elements, (n.d.).

[33] H. Dong, W. Mu, Y. Hu, Q. He, B. Fu, H. Xue, Y. Qin, G. Jian, Y. Zhang, S. Long, Z. Jia, H. Lv, Q. Liu, X. Tao, and M. Liu, "C-V and J-V investigation of HfO_2/Al_2O_3 bilayer dielectrics MOSCAPs on (100) β-Ga_2O_3," AIP Adv. **8**(6), 065215 (2018).

[34] T. Oshima, M. Hashikawa, S. Tomizawa, K. Miki, T. Oishi, K. Sasaki, and A. Kuramata, "β-Ga_2O_3 -based metal–oxide–semiconductor photodiodes with HfO_2 as oxide," Appl. Phys. Express **11**(11), 112202 (2018).

[35] J. Y. Yang, J. Ma, and G. Yoo, "ALD grown polycrystalline HfO_2 dielectric layer on (−201) β-Ga_2O_3 for MOS capacitors," Results Phys. **17**, 103119 (2020).

[36] Ginestra user guide, (n.d.).

[37] E. Caruso, J. Lin, S. Monaghan, K. Cherkaoui, F. Gity, P. Palestri, D. Esseni, L. Selmi, and P. K. Hurley, "The role of oxide traps aligned with the semiconductor energy gap in MOS systems," IEEE Trans. Electron Devices **67**(10), 4372–4378 (2020).

[38] J. Strand, P. La Torraca, A. Padovani, L. Larcher, and A. L. Shluger, "Dielectric breakdown in HfO_2 dielectrics: Using multiscale modeling to identify the critical physical processes involved in oxide degradation," J. Appl. Phys. **131**(23), 234501 (2022).

[39] G. Ribes, S. Bruyere, D. Roy, C. Parthasarthy, M. Muller, M. Denais, V. Huard, T. Skotnicki, and G. Ghibaudo, "Origin of Vt instabilities in high-k dielectrics Jahn–Teller effect or oxygen vacancies," IEEE Trans. Device Mater. Reliab. **6**(2), 132–135 (2006).

[40] P. D. Lomenzo, Q. Takmeel, S. Moghaddam, and T. Nishida, "Annealing behavior of ferroelectric Si-doped HfO_2 thin films," Thin Solid Films **615**, 139–144 (2016).

[41] A. Kumar, J. Y. Lee, and S. Y. Lee, "Phase transformation of sputtered hafnium oxide by post annealing treatment and its effect on the amorphous Si-In-Zn-O thin film transistor," J. Alloys Compd. **906**, 164289 (2022).

[42] J. Strand, M. Kaviani, V. V. Afanas'ev, J. G. Lisoni, and A. L. Shluger, "Intrinsic electron trapping in amorphous oxide," Nanotechnology **29**(12), 125703 (2018).

[43] F. El Kamel, P. Gonon, C. Vallée, and C. Jorel, "Electrode effects on the conduction mechanisms in HfO_2-based metal-insulator-metal capacitors," J. Appl. Phys. **106**(6), 064508 (2009).

[44] H.-S. Lee, J. A. Bain, S. Choi, and P. A. Salvador, "Electrode influence on the transport through $SrRuO_3$/Cr-doped $SrZrO_3$/metal junctions," Appl. Phys. Lett. **90**(20), 202107 (2007).

[45] F. V. Lupo, M. Mosca, S. Bagdzevicius, R. Rani, W. Maudez, E. Wagner, M. P. Casaletto, S. Basile, G. Benvenuti, I. Crupi, and R. Macaluso, "HfO_2 thin films by chemical beam vapor deposition for large resistive switching memristors," IEEE J. Electron Devices Soc. **12**, 508–515 (2024).

[46] L. Baumgarten, T. Szyjka, T. Mittmann, M. Materano, Y. Matveyev, C. Schlueter, T. Mikolajick, U. Schroeder, and M. Müller, "Impact of vacancies and impurities on ferroelectricity in PVD-and ALD-grown HfO_2 films," Appl. Phys. Lett. **118**(3), 032903 (2021).

[47] B. D. Beamson G, *High Resolution XPS of Organic Polymers—The Scienta ESCA 300 Database* (John Wiley & Sons, Chichester, 1992).

[48] J. F. Moulder, W. F. Stickle, P. E. Sobol, and K. D. Bomben, *Handbook of X-Ray Photoelectron Spectroscopy* (Perkin-Elmer Corporation, Eden Prairie, MN, 1992).

[49] W.-C. Cheng, J. He, M. He, Z. Qiao, Y. Jiang, F. Du, X. Wang, H. Hong, Q. Wang, and H. Yu, "Low trap density of oxygen-rich HfO_2/GaN interface for GaN MIS-HEMT applications," J. Vac. Sci. Technol. B **40**(2), 022212 (2022).

[50] W. M. Haynes, *CRC Handbook of Chemistry and Physics* (CRC Press, 2016).

[51] C. Tang and R. Ramprasad, "Point defect chemistry in amorphous HfO_2: Density functional theory calculations," Phys. Rev. B **81**(16), 161201 (2010).

[52] E. Cho, B. Lee, C.-K. Lee, S. Han, S. H. Jeon, B. H. Park, and Y.-S. Kim, "Segregation of oxygen vacancy at metal-HfO_2 interfaces," Appl. Phys. Lett. **92**(23), 233118 (2008).

[53] M. C. Biesinger, C. Brown, J. R. Mycroft, R. D. Davidson, and N. S. McIntyre, "X-ray photoelectron spectroscopy studies of chromium compounds," Surf. Interface Anal. **36**(12), 1550–1563 (2004).

[54] G. Greczynski, D. Primetzhofer, and L. Hultman, "Reference binding energies of transition metal carbides by core-level x-ray photoelectron spectroscopy free from Ar+ etching artefacts," Appl. Surf. Sci. **436**, 102–110 (2018).

[55] R. Jha, J. Chung, B. Chen, R. Nemanich, and V. Misra, "A systematic approach of understanding and retaining pmos compatible work function of metal electrodes on HfO_2 Gate dielectrics," MRS Proc. **917**, 405 (2006).

[56] H. B. Do, Q. H. Luc, M. T. H. Ha, S. H. Huynh, T. A. Nguyen, Y. C. Lin, and E. Y. Chang, "Study of the interface stability of the metal (Mo, Ni, Pd)/HfO_2/AlN/InGaAs MOS devices," AIP Adv. **7**(8), 085208 (2017).

[57] F. Cerbu, O. Madia, D. V. Andreev, S. Fadida, M. Eizenberg, L. Breuil, J. G. Lisoni, J. A. Kittl, J. Strand, A. L. Shluger, V. V. Afanas'ev, M. Houssa, and A. Stesmans, "Intrinsic electron traps in atomic-layer deposited HfO_2 insulators," Appl. Phys. Lett. **108**(22), 222901 (2016).

[58] C. Palade, A.-M. Lepadatu, A. Slav, O. Cojocaru, A. Iuga, V. A. Maraloiu, A. Moldovan, M. Dinescu, V. S. Teodorescu, T. Stoica, and M. L. Ciurea, "A nanoscale continuous transition from the monoclinic to ferroelectric orthorhombic phase inside HfO_2 nanocrystals stabilized by HfO_2 capping and self-controlled Ge doping," J. Mater. Chem. C **9**(36), 12353–12366 (2021).

[59] X.-Y. Zhang, C.-H. Hsu, S.-Y. Lien, W.-Y. Wu, S.-L. Ou, S.-Y. Chen, W. Huang, W.-Z. Zhu, F.-B. Xiong, and S. Zhang, "Temperature-dependent HfO_2/Si interface structural evolution and its mechanism," Nanoscale Res. Lett. **14**(1), 83 (2019).

[60] N. Miyata, "Study of direct-contact HfO_2/Si interfaces," Materials **5**(3), 512–527 (2012).